RSC Advances

ROYAL SOCIETY OF CHEMISTRY

PAPER

View Article Online
View Journal | View Issue

Cite this: *RSC Adv.*, 2021, **11**, 29507

A novel $BiVO_3/SnO_2$ step S-scheme nano-heterojunction for an enhanced visible light photocatalytic degradation of amaranth dye and hydrogen production

Hisham S. M. Abd-Rabboh,[ab] A. H. Galal,[bc] Rafi Abdel Aziz[b] and M. A. Ahmed *[b]

The destruction of toxic pollutants and production of hydrogen gas on the surface of semiconductors under light irradiation is the main significance of photocatalysis. Heterojunctions with matching in band gap energy are urgently required for enhancing the redox power of the charge carriers. A step S-scheme $BiVO_3/SnO_2$ nano-heterojunction was carefully synthesized for a successful photodegradation of amaranth dye and photocatalytic hydrogen evolution. Tetragonal SnO_2 nanoparticles of 80 m^2 g^{-1} surface area and distinct mesoporous structure were fabricated by a sol–gel route in the presence of Tween-80 as the pore structure directing agent. $BiVO_3$ nanoparticles were deposited homogeneously on the SnO_2 surface in an ultrasonic bath of power intensity 300 W. The photocatalytic efficiency in the destruction of amaranth dye soar with increasing $BiVO_3$ contents of up to 10 wt%. The hydrogen evolution rate reached 8.2 mmol g^{-1} h^{-1}, which is eight times stronger than that of pristine SnO_2. The sonicated nanocomposites were investigated by XRD, BET, FESEM, HRTEM, EDS, DRS and PL techniques. The step S-scheme heterojunction with superior oxidative and reductive power is the primary key for the exceptional photocatalytic process. The PL of terephthalic acid and the scavenger trapping experiments reveal the charge migration through the step S-scheme mechanism rather than the type (II) heterojunction mechanism.

Received 18th June 2021
Accepted 26th July 2021

DOI: 10.1039/d1ra04717e

rsc.li/rsc-advances

1. Introduction

Photocatalysis achieving water splitting, organic waste removal and the reduction of CO_2 under light irradiation is a promising route for solving the energy and environmental crisis.[1–6] The broadband light absorption and matching in the band-edge potentials of two different semiconductors is the first challenge in constructing successful heterojunctions. Various semiconductors are extensively investigated for the photodegradation of organic pollutants and photocatalytic hydrogen production.[7–14] SnO_2 with 3.5 eV band gap energy, good optical properties and definite pore structures is a promising candidate for various photocatalytic processes. However, the wide band gap energy, the lower quantum efficiency of charge carriers and the photocatalytic response in the UV region only are negative factors in optimizing its photocatalytic reactivity.[15–20] Bismuth vanadate nanoparticles possess high stability, non-toxicity, rapid formation of the electron–hole pairs by photo-excitation and negative reduction potentials.[21–29] The construction of tin oxide–bismuth vanadate heterojunctions is a hot issue in photocatalytic reactions that facilitate the charge transportation and produce charge carriers with strong redox power. Various charge migration models are postulated for charge migration between two semiconductors, such as type II heterojunction, direct Z-scheme and step S-scheme mechanisms.[30–37] The compatibility in band gap energy of SnO_2 and $BiVO_3$ facilitates the charge migration through the step S-scheme mechanism that involves the removal of the unnecessary electrons and holes of low potential and preserves charge carriers with strong potential for successful redox reactions. The construction of a step-scheme (S-scheme) heterojunction with superior redox ability is an efficient route to develop high-efficiency photocatalysts for various industrial and environmental applications.[38–49] Meng *et al.* prepared TiO_2/polydopamine nanocomposites with a considerably high efficiency in the reduction of CO_2 due to the effective charge carrier separation through the step S-scheme mechanism.[40] The photocatalytic removal of Hg^0 under visible light is reported by Xiao *et al.* on the surface of the CeO_2/BiOI S-scheme heterojunction who reported that the electron migration process through the step S-scheme mechanism enhances the reactivity in the removal process.[41] Li *et al.* incorporated Au on the surface of 2D/2D

[a]*Chemistry Department, Faculty of Science, King Khalid University, PO Box 9004, Abha 61413, Saudi Arabia*

[b]*Department of Chemistry, Faculty of Science, Ain Shams University, Abbassia, Cairo 11566, Egypt. E-mail: abdelhay71@hotmail.com; Fax: +20 224831836; Tel: +20 103979568*

[c]*Chemical Engineering Department, The British University in Egypt, Egypt*

Bi_2MoO_6/g-C_3N_4 for photodegradation of rhodamine B dye through the step-scheme (S-scheme) route.[42] Shaheer *et al.* indicated that photocatalytic hydrogen production on the surface of RGO supported TiO_2/$In_{0.5}WO_3$ is 12 fold higher than that on pristine TiO_2.[43] Wu *et al.* reported that oxygen vacancies activate a new S-scheme heterojunction photocatalyst built from BiOCl.[44] The novel S-scheme heterojunction photocatalysts exhibit an exceptional photocatalytic efficiency in removing aqueous diclofenac (DCF) and gaseous nitric oxide (NO) under visible light irradiation compared with pristine $CuBi_2O_4$ and BiOCl due to the enhanced charge separation and redox ability by the S-scheme heterojunction structure. The reduction in the electron–hole recombination through the step S-scheme mechanism is proposed for photocatalytic hydrogen production on the surface of TiO_2/$SrTiO_3$ synthesized by a hydrothermal process.[49] To our recent knowledge, no research was carried out on construction of step S-scheme $BiVO_3$/SnO_2 heterojunctions through the sonochemical process. The sonochemical route for dispersion of $BiVO_3$ on the SnO_2 surface is an efficient way for enhancing the chemical interaction between two semiconductors over the traditional routes such as impregnation, hydrothermal and solid state processes that weaken the modes of interaction and block the pore structure. The sonochemical route is a green way for fabricating nanocomposites due to its low cost, manipulation of definite particle size and structure, and possibility of producing large-scale products. The as-synthesized heterojunctions were characterized by XRD, HRTEM, N_2-adsorption–desorption isotherm, XPS, DRS and PL analysis. The photocatalytic efficiency of the as-synthesized step S-scheme heterojunctions was investigated by following the photodegradation of amaranth, fluorescein and rhodamine B dyes and hydrogen evolution under simulated solar radiation.

2. Materials and methods

2.1. Materials

Stannic chloride pentahydrate, Tween-80, bismuth nitrate, sodium vanadate, ammonia solution, absolute ethanol, methanol, amaranth dye, isopropanol, benzoquinone, ammonium oxalate and terephthalic acid were purchased from Sigma-Aldrich Company with purity = 99%.

2.2. Preparation of SnO_2 nanoparticles

25 ml of Tween-80 dissolved in 50 ml isopropanol and 80 ml of ethylene glycol was added to 20 g of stannic chloride dissolved in isopropanol solution followed by vigorous stirring for three hours. $Sn(OH)_4$ sol was formed by adding ammonia solution [1 M] with constant stirring for 3 with precise adjustment of the pH of the mixture at 8. At the last stage of preparation, the resulting sol was filtered, washed several times with distilled water to remove chloride ions, dried overnight at 100 °C and calcined for 10 hours at 460 °C.

2.3. Preparation of $BiVO_3$ nanoparticles

Bismuth nitrate and sodium monovanadate were dissolved in ethylene glycol and mixed together with equal concentration in an ultrasonic bath of 300 W for 45 minutes. Afterwards, the sol is filtered, washed with distilled water several times and dried at 140 °C for 24 hours.

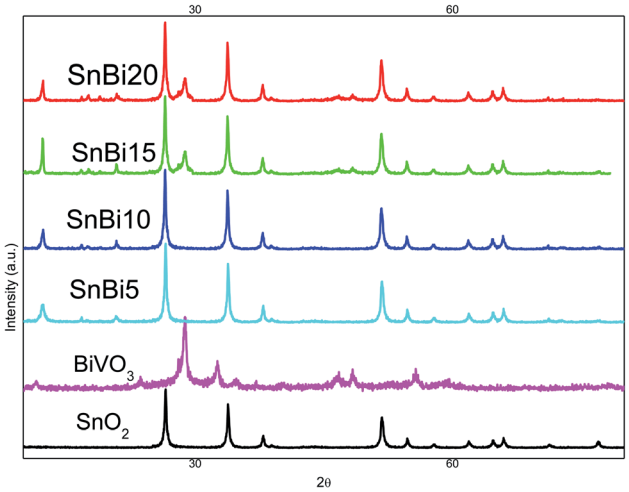

Fig. 1 (a) XRD of SnO_2, $BiVO_3$, $SnBi_5$, $SnBi_{10}$, $SnBi_{15}$ and $SnBi_{20}$.

2.4. Preparation of $BiVO_3$/SnO_2 nanoparticles

A definite amount of bismuth nitrate dissolved in ethylene glycol was mixed with SnO_2 nanoparticles with constant stirring for three hours in a certain ratio in an attempt to obtain (5, 10, 15 and 20 w/w%) $BiVO_3$/SnO_2. Then, a stoichiometric amount of sodium monovanadate dissolved in ethylene glycol was added to the above solution and placed in an ultrasonic bath with an intensity of 300 W for one hours. The above sol mixture is filtered, washed with distilled water and dried at 80 °C for 24 hours. The bare samples are denoted as SnO_2 and $BiVO_3$ and the samples denoted as $SnBi_5$, $SnBi_{10}$, $SnBi_{15}$ and $SnBi_{20}$ correspond to the nanocomposite containing 5, 10, 15 and 20 wt% of $BiVO_3$ contents.

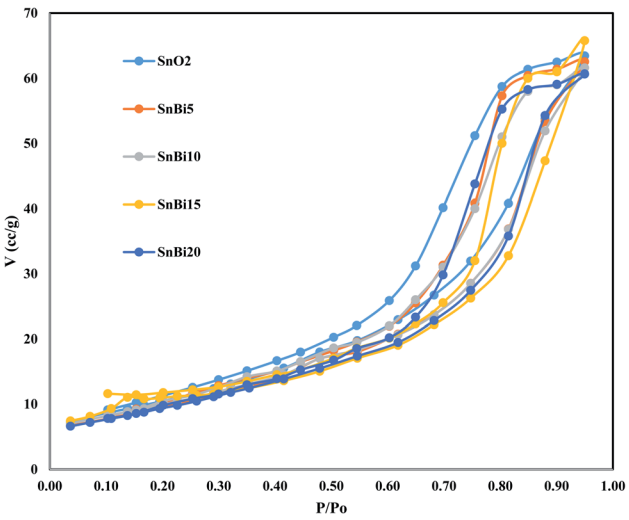

Fig. 2 N_2-adsorption–desorption isotherm of SnO_2, $BiVO_3$, $SnBi_5$, $SnBi_{10}$, $SnBi_{15}$ and $SnBi_{20}$.

2.5. Material characterization

A PANalytical X'PERT MPD diffractometer using (Cu [$K\alpha_1/K\alpha_2$]) radiation was employed for recording the crystalline parameters. The surface area and the pore structure were recorded by adsorption isotherms of N_2 at 77 K using a volumetric technique. High resolution transmission electron microscope features were estimated with an HRTEM JEOL 6340. XPS studies were carried out using a K-ALPHA (Thermo Fisher Scientific, USA) instrument with monochromatic X-ray Al Kα radiation from 10 to 1350 eV. Diffuse reflectance spectra were detected with a JASCO spectrometer (V-570). The photocatalytic power for amaranth dye destruction on the as-synthesized heterojunctions was recorded under a solar simulator. The photocatalytic degradation of pollutant dye models such as amaranth, rhodamine and fluorescein dyes was carried out over the surface of 0.1 g of the as-synthesized photocatalyst in a glass reactor under a xenon lamp of intensity 300 W. The photodegradation of dye involves mixing 0.1 g of the sample with 100 ml of dye solution of concentration 5×10^{-5} M fluorescein and amaranth dye and 2×10^{-5} with respect to rhodamine B dye, then the mixture was kept stirring for 60 min in dark to attain the adsorption–desorption equilibrium of dye on the photocatalyst surface. After equilibration, the concentration of the dye in terms of absorbance was measured using a Thermo Scientific Evolution 300 UV-vis spectrophotometer and the result was taken as the initial concentration (C_0) of the dye. Then, a xenon lamb was switched on over the suspension and at different irradiation time intervals, 5 ml of dye solution was withdrawn and analyzed using a UV-vis spectrophotometer to determine the residual concentration (C_t) of the dye. Finally, the photocatalytic activity percentage of each sample was calculated using the following equation:

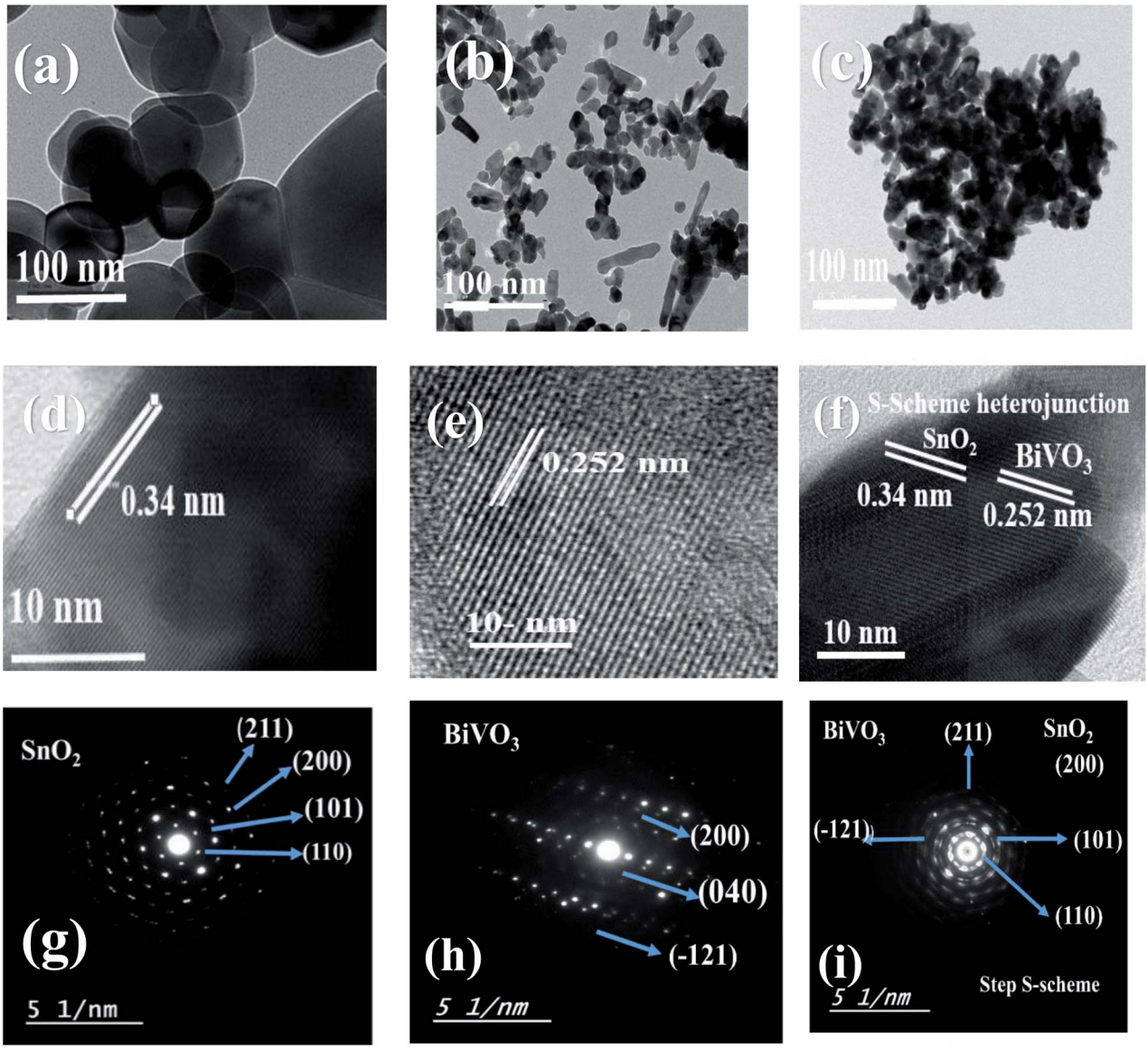

Fig. 3 TEM of (a) SnO_2, (b) $BiVO_3$, and (c) $SnBi_{10}$, (d) HRTEM of (d) SnO_2, (e) $BiVO_3$, and (f) $SnBi_{10}$, and SAED of (g) SnO_2, (h) $BiVO_3$, and (i) $SnBi_{10}$.

$$\text{Photocatalytic activity } \% = (C_t/C_0) \times 100$$

The concentration of the hydroxyl groups was estimated by following the production of 2-hydroxyterephthalic acid [2-HTA] at a defined emission signal with 423 nm wavelength. The proportion of hydrogen gas evolved was detected under a 300 W xenon lamp in a glass reactor. The as-synthesized samples were suspended into 150 ml of methanol solution. After 1 h illumination, 500 μL gaseous products were taken from the reactor and then measured by gas chromatography.

3. Results and discussion

3.1. Physicochemical characterization

The diffraction pattern of pristine SnO_2 shows prevailing diffraction peaks at $2\theta = 26.6$, 34.2, 37.6, 51.8, 54.8, 58.4, 61.9 and 65.2° referred to the cassiterite tetragonal (rutile type) structure of SnO_2 (ICDD card no.41-1445) of space group $P4_2/mnm$. The XRD pattern of $BiVO_3$ nanoparticles shows pronounced diffraction peaks at $2\theta = 12.7$, 28.88, 30.38, 34.7, 35.4, 39.9, 42.6, and 53.22° marked by their miller indices [(−121), (040), (200), (002), (211) and (051)] related to monoclinic $BiVO_3$ crystallites. By carefully noticing the XRD spectrum, the diffraction peak at $2\theta = 12.7°$ referred to $BiVO_3$ is shifted to 13.7° upon incorporation of $BiVO_3$ on the surface of SnO_2 nanoparticles. This change in the position of the diffraction peak of $BiVO_3$ can be ascribed to the strong interaction between SnO_2 and $BiVO_3$ that induces some change in the crystalline parameters. The crystallite size estimated by the Debye–Scherrer equation is 42, 54, 33, 25, 19 and 13 nm for SnO_2, $BiVO_3$, $SnBi_5$, $SnBi_{10}$, $SnBi_{15}$ and $SnBi_{20}$, respectively (Fig. 1). With incorporation of $BiVO_3$ nanoparticles on the SnO_2 surface, the crystallite size was drastically reduced, reflecting the favorable dispersion of $BiVO_3$ nanoparticles between SnO_2 crystallites decreasing their dimensions.

The porosity and the surface structure of the as-synthesized heterojunctions are verified by N_2 adsorption–desorption isotherms at 77 K on SnO_2, $SnBi_5$, $SnBi_{10}$, $SnBi_{15}$ and $SnBi_{20}$ (Fig. 2). These isotherms are referred to type IV with H1 hysteresis loop, indicating the cylindrical pore structure that facilitates the free movement of reactant molecules. The surface area determined from the BET equation is 108, 91, 78, 65 and 56 $m^2\ g^{-1}$ for SnO_2 $SnBi_5$, $SnBi_{10}$, $SnBi_{15}$ and $SnBi_{20}$, respectively.

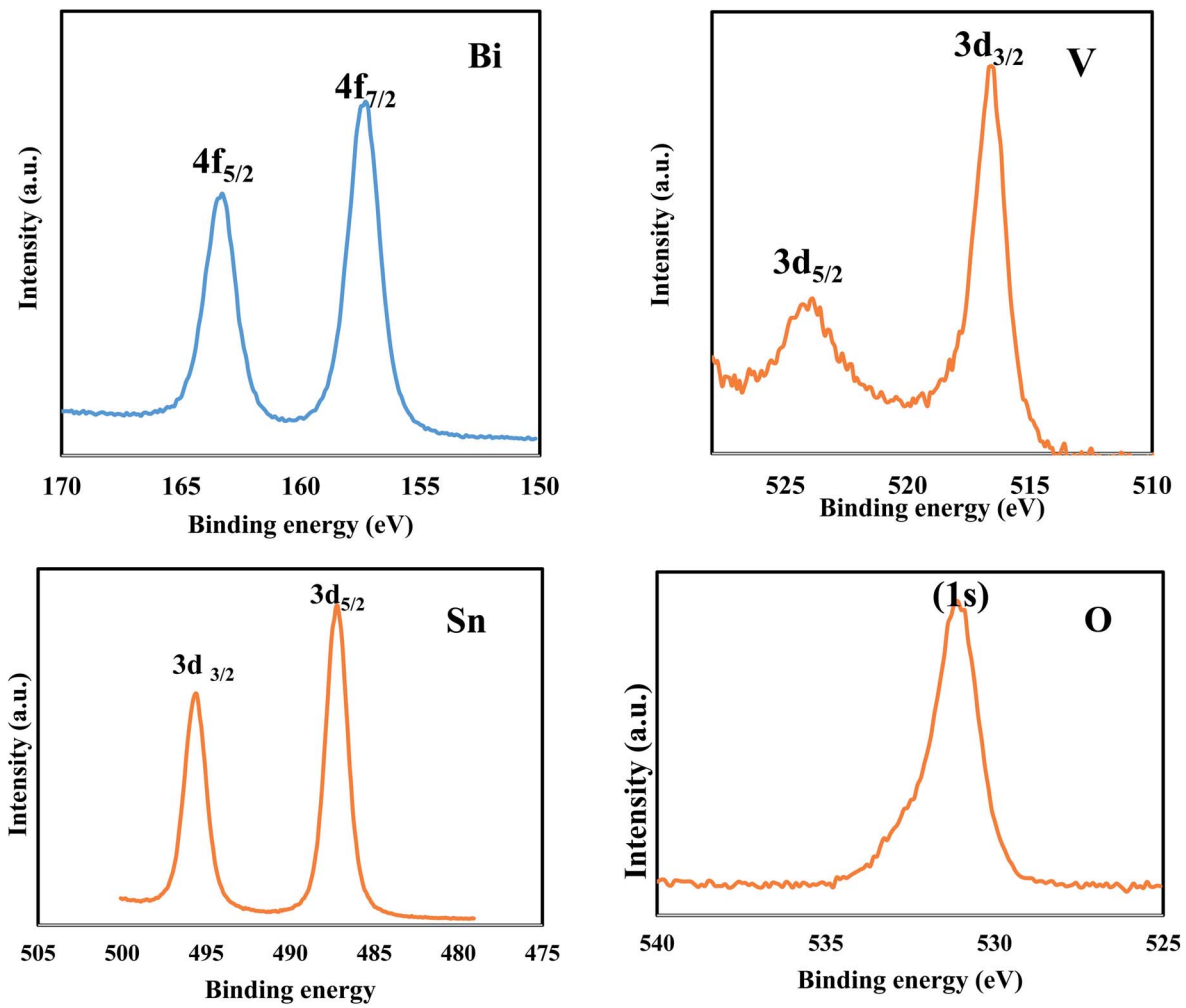

Fig. 4 XPS of Sn, O, Bi and V in $SnBi_{10}$.

With incorporation of various concentrations of $BiVO_3$, the surface area and hysteresis loop size are much reduced due to deposition of $BiVO_3$ nanoparticles on the outer surface and inside the pore structure of SnO_2 blocking a large number of active sites available for attracting N_2-molecules.

Fig. 3 illustrates the TEM images of (a) SnO_2, (b) $BiVO_3$ and (c) $SnBi_{10}$ nanoparticles. It is clearly observed that the homogeneous dispersion of $BiVO_3$ covers the SnO_2 matrix. Fig. 3d–f reveals the formation of a $BiVO_3$–SnO_2 heterojunction through production of a crystalline plane of 0.34 nm referred to the (111) plane of tetragonal SnO_2 and 0.255 referred to the (111) plane of monoclinic $BiVO_3$. SAED analysis shows various diffraction rings at (110), (101), (200), (211) and (220) planes belonging to tetragonal SnO_2 nanoparticles [Fig. 3g–i]. On the other hand, the different diffraction rings at (−121), (040), (200) and (002) are referred to $BiVO_3$ crystal. HRTEM and SAED experimental results are clear evidence for construction of a step S-scheme $BiVO_3$–SnO_2 heterojunction that not only enhances the separation of the charge carriers, but also improves the oxidative and reductive power of the solid sample.

The precise elemental composition and the oxidation state of elements in the constructed $BiVO_3/SnO_2$ step S-scheme heterojunction are investigated by XPS analysis. The spectrum displays two sharp peaks at 486 and 495.6 eV belonging to Sn $3d_{3/2}$ and Sn $3d_{5/2}$, respectively (Fig. 4). The binding energies of 516.7 and 524.0 eV are referred to V $2p_{3/2}$ and V $2p_{5/2}$ in $BiVO_3$/SnO_2 for the V^{5+} oxidation state. The asymmetric O 1s at a binding energy of 530 eV indicates the presence of oxygen. The binding energies of 158.5 and 164.4 eV are referred to $4f_{7/2}$ and $4f_{5/2}$ of Bi^{3+}.

The DRS spectrum shows an absorption band edge at 400 nm referred to SnO_2 nanoparticles; however, a prevailing band edge at 580 nm points to the absorption characteristics of $BiVO_3$ in the visible region [Fig. 5a]. $BiVO_3$ nanoparticles are beneficial for the light harvesting and the enhancement of the utilization of solar light by shifting the absorption features to higher wave length. The band gap energy [E_g] calculated from the Tauc equation is 3.20, 2.2, 3.1, 2.95 and 2.81 eV for the pristine SnO_2, $BiVO_3$, $SnBi_5$, $SnBi_{10}$ and $SnBi_{15}$, respectively [Fig. 5b].

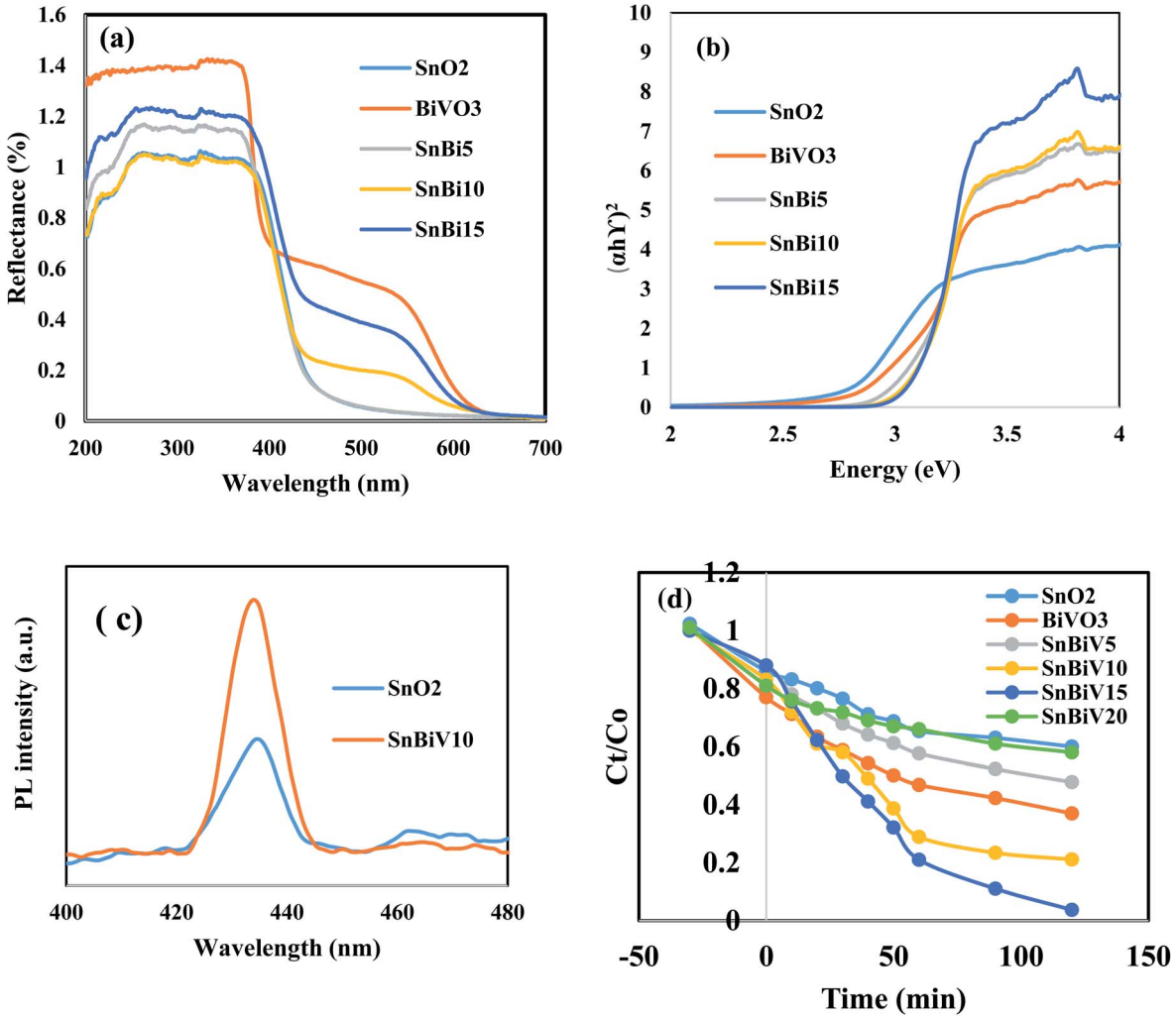

Fig. 5 (a) DRS of SnO_2, $BiVO_3$, $SnBi_5$, $SnBi_{10}$, $SnBi_{15}$ and $SnBi_{20}$, (b) Tauc plot for SnO_2, $BiVO_3$, $SnBi_5$, $SnBi_{10}$, $SnBi_{15}$ and $SnBi_{20}$, (c) PL of SnO_2 and $SnBi_{10}$, (d) Photodegradation of amaranth dye over SnO_2 containing various proportions of $BiVO_3$.

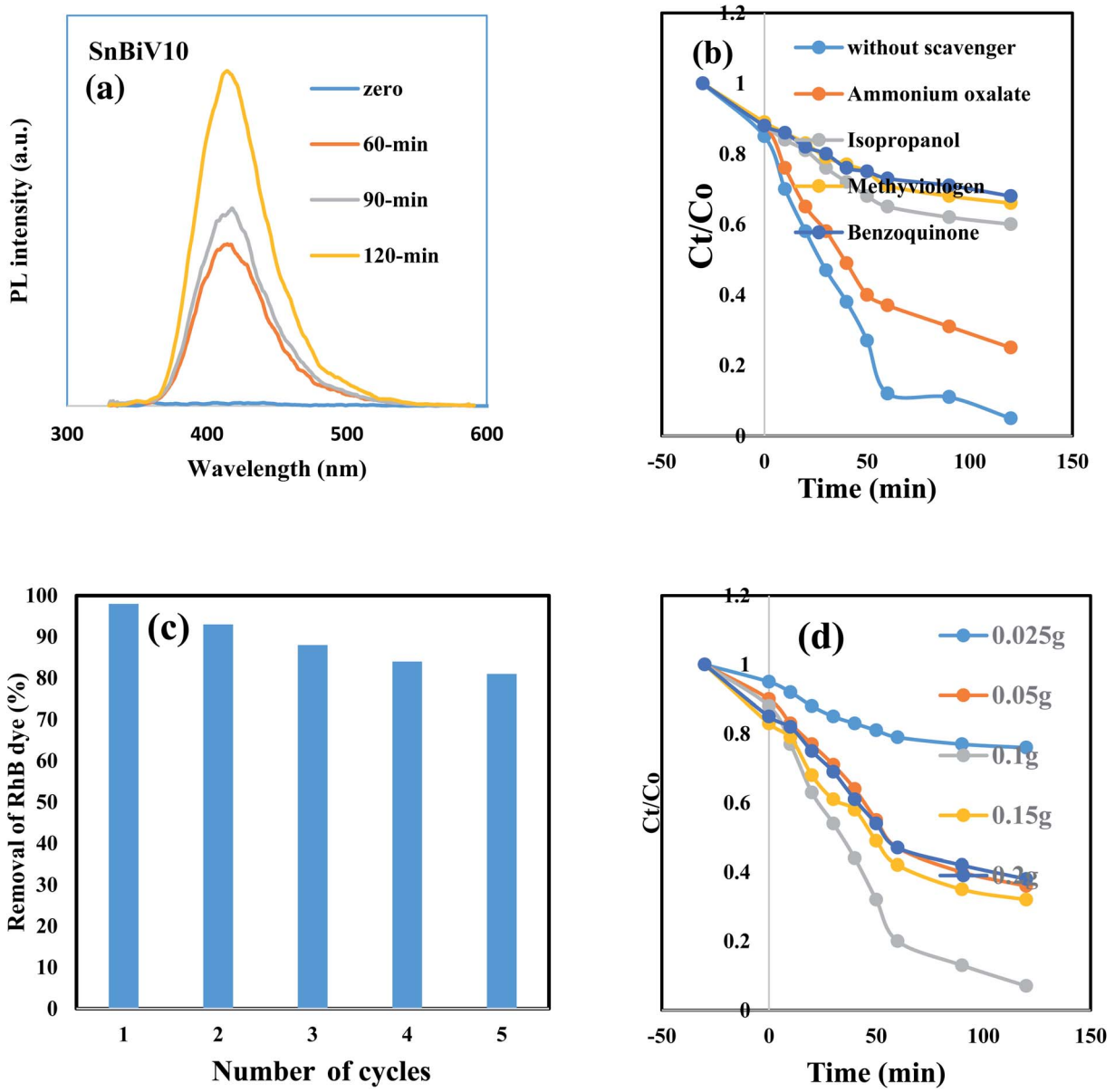

Fig. 6 (a) PL of terephthalic acid over $SnBi_{10}$, (b) effect of various scavengers over $SnBi_{10}$, (c) effect of regeneration of $SnBi_{10}$ on the removal of amaranth dye, and (d) effect of photocatalyst weight on the removal of amaranth dye.

The valence and conduction band edges at the point of zero charge of the semiconductor were estimated from the following equation:

$$E_{VB} = X - E_e + 0.5E_g$$

$$E_{CB} = E_{VB} - E_g$$

where X is the semiconductor electronegativity which is 6.5 and 5.7 eV for $BiVO_3$ and SnO_2 respectively. E_e is the energy of free electrons on the hydrogen scale (4.5 eV). Based on the above equations, SnO_2 has the conduction band potential $E_{CB} = -0.4$ eV and valence band potential $E_{VB} = +2.8$ eV; however, $BiVO_3$ has the conduction band potential $E_{CB} = +0.9$ eV and valence band potential $E_{VB} = +3.1$ eV. The synergetic effect between SnO_2 and $BiVO_3$ facilitates step S-scheme heterojunction construction through which charges' transfer as well as the positive holes and electrons in the inferior energy levels are consumed. However, a high negative and positive potential of SnO_2 conduction and valence band of $BiVO_3$ are preserved with strong reduction and oxidation power. The quantum efficiency of charge carrier separation is further highlighted by the photoluminescence [PL] spectrum. The reduction in the prevailing signal intensity at 435 nm of SnO_2 crystalline defects [Fig. 5c] reflects the strong quantum power of $BiVO_3$ in promoting the efficiency of the charge carrier separation in the novel heterojunction.

3.2. Photocatalytic degradation of amaranth dye

Amaranth dye is extensively used in industry and causes various environmental problems and health issues such as headaches,

tumors, allergies, and other health problems after long periods of exposure. Amaranth dye with a complex aromatic structure is difficult to degrade by traditional methods. We select amaranth dye to compare the photocatalytic efficiency of the as-synthesized heterojunctions. The reactivity of the pristine SnO_2 and $BiVO_3$ is very low under solar radiation due to the wide band gap energy of SnO_2 and the rapid recombination of the charge carriers in $BiVO_3$ nanoparticles. The photocatalytic power soars rapidly with incorporating $BiVO_3$ on the SnO_2 surface and reached an optimal efficiency for the heterojunction embedded 10 wt% $BiVO_3$. The decrease in the photocatalytic reactivity from degrading 92% of amaranth dye to 62% on increasing $BiVO_3$ content from 15 to 20 wt% results from the production of several $BiVO_3$ crystalline layers coating the SnO_2 surface and hindering the light penetration on the photocatalyst surface. These results indicate that the amount of $BiVO_3$ in the nanocomposite plays a crucial role in controlling the removal of amaranth dye [Fig. 5d]. The dye degradation pseudo first order rate is 0.0023, 0.0063, 0.008, 0.0072, 0.023 and 0.0033 over SnO_2, $BiVO_3$, $SnBi_5$, $SnBi_{10}$, $SnBi_{15}$ and $SnBi_{20}$, respectively. The photocatalytic route is more efficient in removal of amaranth dye rather than the adsorption process that weakens the degradation process due to blocking of the active centers by dye molecules and reduces the catalyst durability. Hydroxyl radical concentration was estimated from measurements of PL of terephthalic acid that records the production of 2-hydroxy terephthalic acid monitored by the formation of a characteristic signal at 423 nm [Fig. 6a]. The reactive species nature that determines the charge migration route for removal of amaranth dye over $SnBi_{10}$ was elucidated by trapping scavengers such as ammonium oxalates, isopropanol, benzoquinone and silver nitrate. Silver nitrate exhibits little effect on the degradation rate, revealing that the electron conduction band plays a small role in dye degradation [Fig. 6b]. The decrease in the photocatalytic efficiency with ammonium oxalate, isopropanol and benzoquinone gives an account on the positive role of hydroxyl radicals, positive holes and superoxide radicals in dye removal. The photocatalytic stability of the prepared nanocomposite was estimated by subjecting the photocatalyst to five consecutive cycles under simulated solar irradiation. After five consecutive

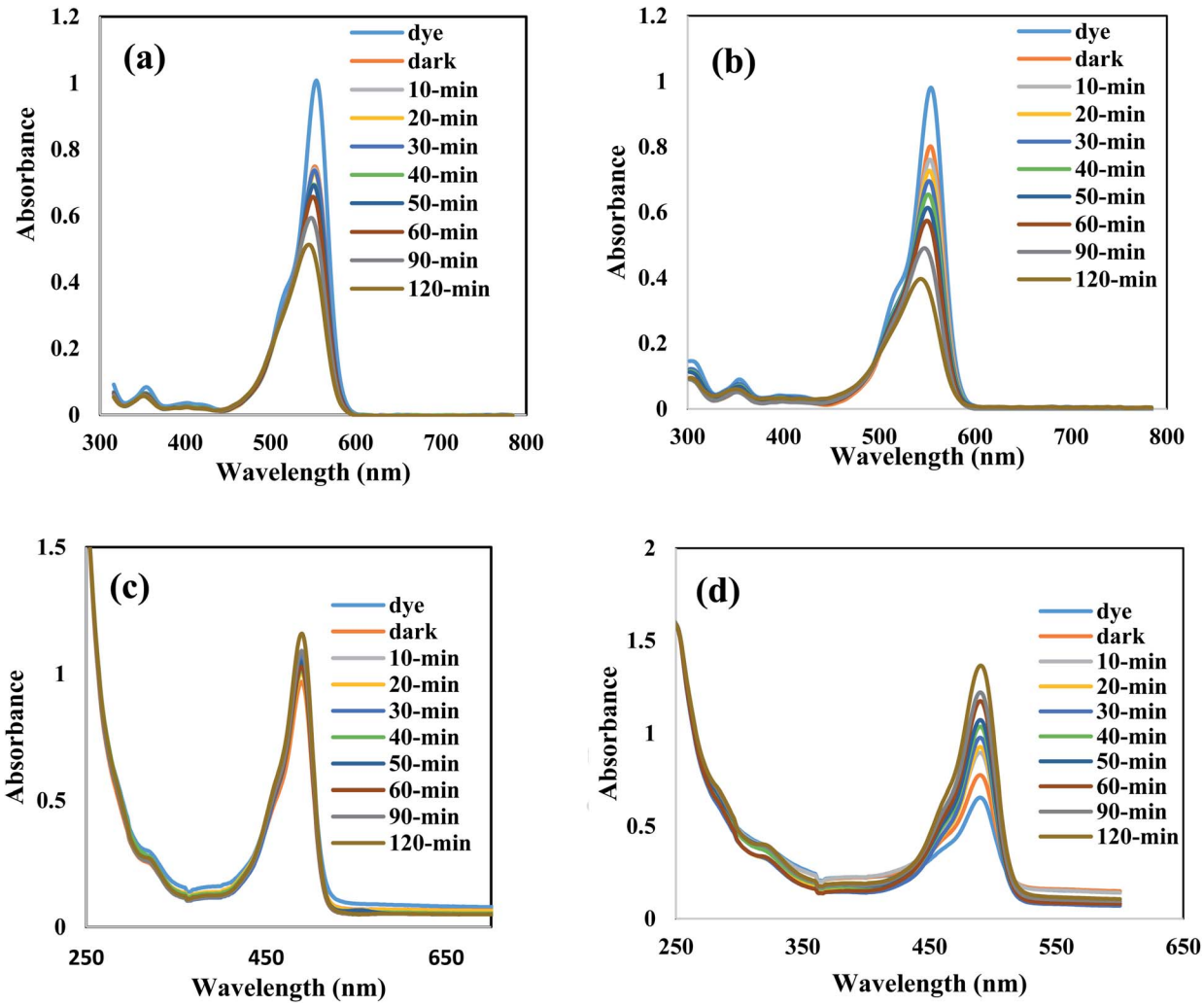

Fig. 7 Absorption spectrum for removal of rhodamine B dye over (a) SnO_2 and (b) $SnBi_{10}$, and absorption spectrum for removal of fluorescein dye over (c) SnO_2 and (d) $SnBi_{10}$.

cycles, the photocatalyst retains 83% of its efficiency [Fig. 6c]. Fig. 6d demonstrates the influence of the photocatalyst weight on the dye degradation that indicates that the optimal value for dye degradation is 0.1 g, responsible for removal of 90% of the dye. TOC is evaluated in the revised manuscript and the TOC is reduced from 85 mg l^{-1} to 9.2 mg l^{-1}, revealing the removal of 90% of the amaranth dye.

The photocatalytic degradation of rhodamine B dye as a cationic pollutant model and fluorescein dye as another anionic pollutant model was carried out on bare SnO_2 and the optimum sample $SnBi_{10}$ to investigate the efficiency of the photocatalyst in degrading different pollutant models [Fig. 7]. The experimental results indicate the removal of 45% of RhB dye on bare SnO_2 compared with 78% removal over the $SnBi_{10}$ surface. On the other hand, removal of 16% of fluorescein dye over bare SnO_2 was observed compared with the 62% removal on the $SnBi_{10}$ surface. This result confirmed the positive role of $BiVO_3$ in improving the photocatalytic efficiency of SnO_2.

The amount of hydrogen gas evolved was tested on the photocatalyst surface embedded different $BiVO_3$ proportions with methanol as the hole scavenger [Fig. 8a]. $BiVO_3$ nanoparticles alone exhibit weak photocatalytic activity due to the rapid recombination of the charge carriers which is the main defect for this material. The amount of hydrogen evolved on the SnO_2 surface reached 2.4 mmol h^{-1} g^{-1} after two hours of the photoreaction. With the incorporation of $BiVO_3$, the photocatalytic hydrogen evolution rate increases rapidly with increasing $BiVO_3$ content. Noticeably, promoted photocatalytic H_2 production activity of 8.6 mmol g^{-1} h^{-1} was achieved for the nanocomposite containing 10 wt% $BiVO_3$ content. The increase in $BiVO_3$ concentration reduces the photocatalytic rate, revealing that there is an optimal value for $BiVO_3$ content. The enhancement in the photocatalytic reactivity can be ascribed to the bifunctional role of $BiVO_3$; one promotes the quantum efficiency of charge separation as proved from PL analysis and another enhances the rate of hydrogen evolution. Probably, HRTEM results reveal that $BiVO_3$ covered SnO_2 nanoparticles by successive layers that may inhibit the migration of positive holes to react with methanol. These holes accumulated in $BiVO_3$ are prone to react with electrons and act as recombination centers. Fig. 8b presents the effect of photocatalyst weight on the amount of photocatalytic hydrogen production. The amount of hydrogen produced reaches a maximum value for 0.05 g of the nanocomposite. The influence of pH on the hydrogen

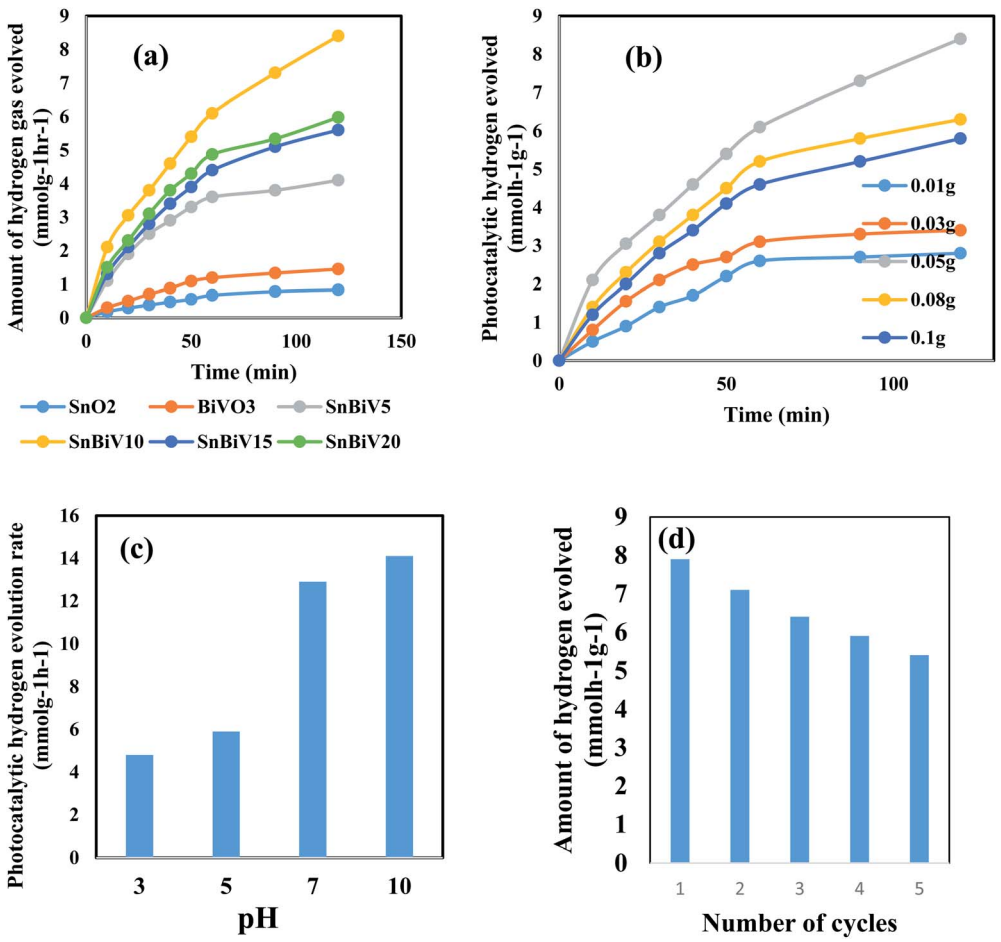

Fig. 8 (a) The influence of amount of $BiVO_3$ on the photocatalytic hydrogen evolution rate (mmol g^{-1} h^{-1}), (b) the effect of weight of the photocatalyst on the amount of hydrogen evolved (mmol g^{-1} h^{-1}), (c) the effect of pH on the photocatalytic hydrogen evolution over $SnBi_{10}$, and (d) the effect of catalyst regeneration on the photocatalytic hydrogen evolution over $SnBi_{10}$.

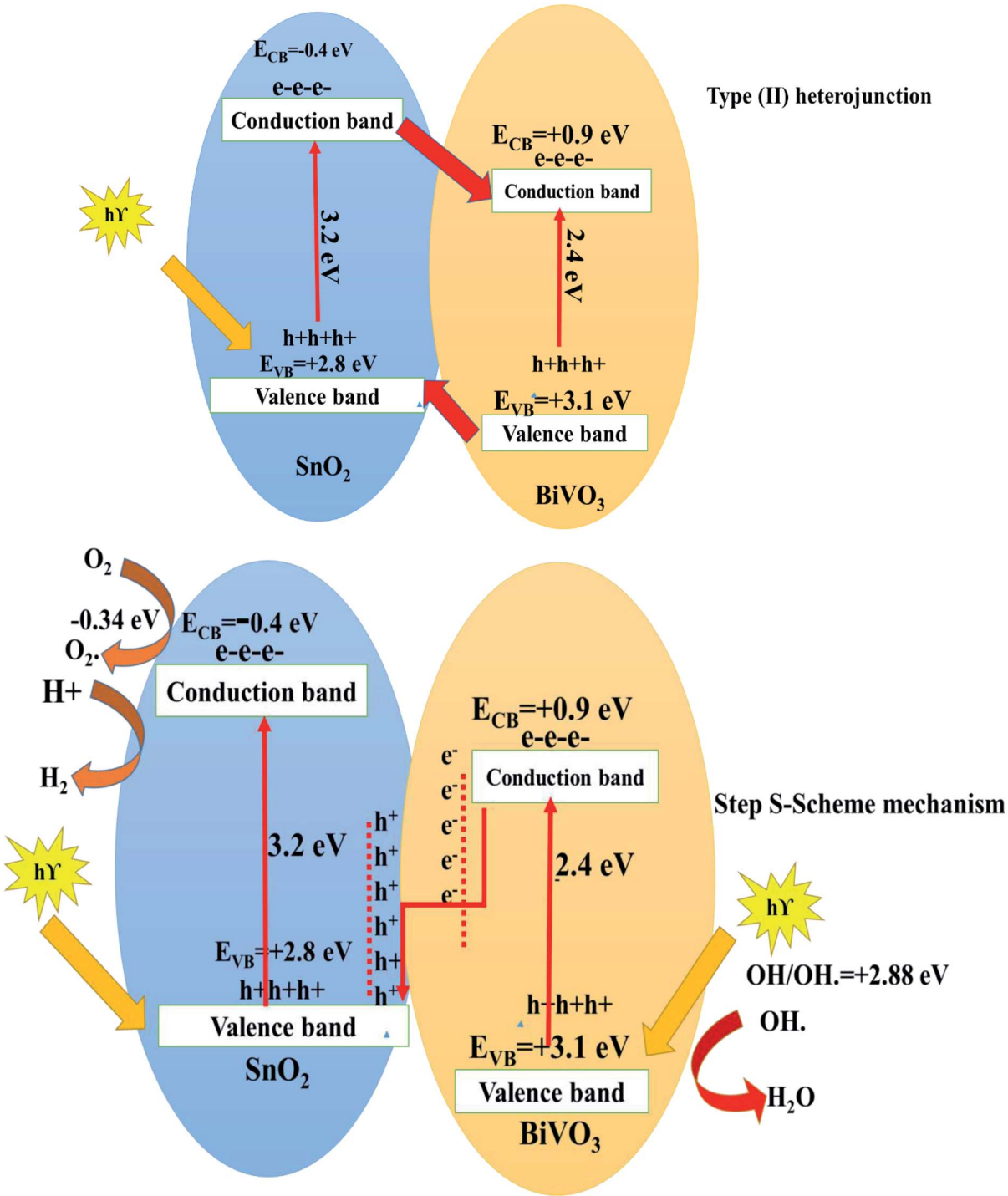

Fig. 9 A scheme for charge transfer between SnO_2 and $BiVO_3$ under solar light.

evolution process is presented in Fig. 8c, revealing that pH = 10 is the optimal value for producing a maximum amount of hydrogen gas. The photostability of the $BiVO_3/SnO_2$ that retains 80% of its reactivity after five consecutive cycles suggests the reusability of these novel nanoparticles in the production of hydrogen gas [Fig. 8d].

Various models discuss the charge migration route between two semiconductors.[32–37] Conventional type-II heterojunctions reduced the redox ability of the photogenerated charge carriers. However, the direct Z-scheme hybrid photocatalyst system that mimics natural photosynthesis preserves both the high reductive and oxidative powers of the photogenerated charge carriers. To remove the defects of the traditional heterojunctions [type-II], and direct Z-scheme photocatalysts, a new step-scheme (S-scheme) heterojunction concept was proposed. The S-scheme heterojunction embedded two n-type semiconductor

photocatalysts. The internal electric field between the two semiconductors is the driving force for the charge transfer process. As a consequence, the electrons and holes are separated in space, located in the CB of the reduction photocatalyst and the VB of the oxidation photocatalyst, respectively. The photocatalytic oxidation and reduction reactions are usually started by these holes and electrons, respectively. An efficient S-scheme heterojunction system is highly favorable, which promotes the charge dynamics and substantially sustains favorable charge potentials.

In this research, adopting the type (II) heterojunction[15,19] involves the electron transfer from the more negative to less negative potential conduction band; however, holes transfer in the opposite direction. Based on the above arguments, electrons transfer from more negative potential SnO_2 to less negative potential $BiVO_3$ conduction band. On the other hand, the holes transfer from $BiVO_3$ to SnO_2 valence band. The potential of the SnO_2 valence band is 2.8 eV which is weak to oxidize water into hydroxyl radicals with a potential of $OH^-/OH = 2.88$ eV.[5,15,19] However, the potential of the $BiVO_3$ conduction band is 0.9 eV which is lower than the reduction potential of hydrogen H^+/H_2. In the light of the above situation, the type II heterojunction cannot explain hydrogen evolution or dye degradation by hydroxyl radicals as it is documented from scavenger experiments. By adopting the step S-scheme mechanism,[38–49] the positive holes in the VB of SnO_2 and electrons in the CB of $BiVO_3$ are sacrificed. However, the positive holes in the VB of $BiVO_3$ with a potential of 3.1 eV easily oxidize water to produce hydroxyl radicals (OH-/OH.) and electrons in the CB of SnO_2 with a potential of -0.5 eV can reduce H^+ to produce hydrogen gas. Fig. 9 displays the step S-scheme mechanism for electron transfer between two semiconductors. The mechanism involves electron transfer from the VB to the CB of both SnO_2 and $BiVO_3$, followed by removal of holes and electrons in the valence and conduction band with lower potential. On the other hand, the holes and electrons in higher valence and conduction bands are maintained with strong oxidative and reductive power. This step S-scheme mechanism is desirable for explaining our experimental data for both dye degradation and hydrogen evolution processes.

4. Conclusions

Herein, we have successfully fabricated a step S-scheme heterojunction composed of SnO_2 and $BiVO_3$ nanoparticles without using an electron mediator. Tetragonal SnO_2 nanoparticles were synthesized by a sol–gel route using Tween-80; afterwards, $BiVO_3$ nanoparticles were incorporated on the SnO_2 surface by a sonochemical route. In particular, there is an optimal value of $BiVO_3$ for enhancing the photocatalytic reactivity which seems to be 10 wt%. DRS and PL studies have demonstrated that the step S-scheme mechanism not only enhances the separation efficiency of charge carriers, but also increases the oxidizing and reducing power of the holes and electrons. The step S-scheme mechanism activates the recombination of the holes and electrons in the lower valence and conduction bands, leaving the holes and electrons in higher energy state preserved with an efficient oxidation power for amaranth dye degradation and strong reducing power for production of hydrogen gas. The controlled efficient species in amaranth dye degradation are positive holes, hydroxyl and superoxide radicals. The novel hybrid nanoparticle retains its reactivity after five consecutive cycles.

Conflicts of interest

The authors declare that there is no conflict of interest in the research work.

Acknowledgements

The authors extend their appreciation to the Deanship of Scientific Research at King Khalid University for funding this work through General Research Project under grant number (RGP.2/145/42).

References

1 M. Beneissa, N. Abbas, A. A. Saleh, N. Elboughdiri, A. Moumen, M. S. Hamdy, H. S. M. Abd-Rabboh, A. H. Galal, M. Gad Al-Metwaly and M. A. Ahmed, $BiVO_3$/g-C_3N_4 S-scheme heterojunction nanocomposite photocatalyst for hydrogen production and amaranth dye removal, *Opt. Mater.*, 2021, **118**, 111237.

2 M. A. Ahmed, A. Fahmy, M. G. Abo-Zaed and E. M. Hashem, Fabrication of novel $AgIO_4/SnO_2$ heterojunction for photocatalytic hydrogen production through direct Z-scheme mechanism, *J. Photochem. Photobiol., A*, 2020, **400**, 112660.

3 Y. Liu, Q. Zhang, M. Xu, H. Yuan, Y. Chena, J. Zhang, K. Luo, J. Zhang and B. You, Novel and efficient synthesis of Ag-ZnO nanoparticles for the sunlight induced photocatalytic degradation, *Appl. Surf. Sci.*, 2019, **476**, 632–640.

4 M. S. Hamdy, H. S. M. Abd-Rabboh, M. Beneissa, M. Gad Al-Metwaly, A. H. Glal and M. A. Ahmed, Fabrication of novel polyaniline/ZnO heterojunction for exceptional photocatalytic hydrogen production and degradation of fluorescein dye through direct Z-scheme mechanism, *Opt. Mater.*, 2021, **117**, 111198.

5 F. A. Fouad, M. A. Ahmed, M. S. Antonious and M. F. Abdel-Messih, Synthesis of an efficient, stable and recyclable $AgVO_3$/ZnO nanocomposites with mixed crystalline phases for photocatalytic removal of rhodamine B dye, *J. Mater. Sci.: Mater. Electron.*, 2020, **31**, 12355–12371.

6 L. Ling, Y. Feng, H. Li, Y. Chen, J. Wen, J. Zhu and Z. Bian, Microwave induced surface enhanced pollutant adsorption and photocatalytic degradation on Ag/TiO_2, *Appl. Surf. Sci.*, 2019, **483**, 772–778.

7 El-H. Hashem, A. Fahmy, A. Abbas, M. Tarek, B. Mahran and M. A. Ahmed, Fabrication of novel $AgIO_4/TiO_2$ heterojunction for photocatalytic hydrogen production through direct Z-scheme mechanism, *Nanotechnol. Environ. Eng.*, 2020, **5**, 17.

8 E. M. Ezz el-regal, M. A. Ahmed, M. F. Abdel-Messih and Z. M. Abou-Gamra, Synthesis of novel ZnO nanoparticles with exceptional crystalline and photocatalytic features toward recalcitrant pollutant: Fluorescein dye, *Opt. Mater.*, 2021, **111**, 110597.

9 Z. M. Abou-Gamra, M. A. Ahmed and M. A. Hamza, Investigation of commercial $PbCrO_4/TiO_2$ for photodegradation of rhodamine B in aqueous solution by visible light, *Nanotechnol. Environ. Eng.*, 2017, **2**, 12.

10 M. A. Ahmed, Z. M. Abou-Gamra and M. A. ALshakhanbeh, Hesham Medien; Control synthesis of metallic gold nanoparticles homogeneously distributed on hexagonal ZnO nanoparticles for photocatalytic degradation of methylene blue dye, *Environ. Nanotechnol. Monit. Manag.*, 2019, **12**, 100217.

11 M. A. Ahmed, F. Ahmed, M. G. Abo-Zaed and E. M. Hashem, Fabrication of novel $AgIO_4/SnO_2$ heterojunction for photocatalytic hydrogen production through direct Z-scheme mechanism, *J. Photochem. Photobiol., A*, 2020, **400**, 112660.

12 M. A. Hamza, Z. M. Abou-Gamra, M. A. Ahmed and H. A. A. Medien, The critical role of Tween 80 as a 'green' template on the physical properties and photocatalytic performance of TiO_2 nanoparticles for Rhodamine B photodegradation, *J. Mater. Sci.: Mater. Electron.*, 2020, **31**, 4650–4661.

13 H. Mao, Z. Fei, C. Bian, L. Yu, S. Chen and Y. Qian, Facile synthesis of high-performance photocatalysts based on Ag/TiO_2 composites, *Ceram. Int.*, 2019, **45**, 12586–12589.

14 M. F. Abdel Messih, A. E. Shalan, M. F. Sanad and M. A. Ahmed, Facile approach to prepare $ZnO@SiO_2$ nanomaterials for photocatalytic degradation of some organic pollutant models, *J. Mater. Sci.: Mater. Electron.*, 2019, **30**, 1491–1499.

15 E. E. El-Katori, M. A. Ahmed, A. A. El-Bindary and A. M. Orab, Impact of CdS/SnO_2 heterostructured nanoparticle as visible light active photocatalyst for the removal methylene blue dye, *J. Photochem. Photobiol., A*, 2020, **392**, 112403.

16 M. F. Abdel-Messih, M. A. Ahmed and A. S. El-Sayed, Structure and Photocatalytic decolorization of Rhodamine B dye using novel mesoporous SnO_2-TiO_2 nano mixed oxides prepared by sol-gel method, *J. Photochem. Photobiol., A*, 2013, **260**, 1–8.

17 M. A. Ahmed, M. F. Abdel Messih, E. F. El-Sherbeny, S. F. El-Hafez and A. M. M. Khalifa, Synthesis of metallic silver nanoparticles decorated mesoporous SnO_2 for removal of methylene blue dye by coupling adsorption and photocatalytic processes, *J. Photochem. Photobiol., A*, 2017, **346**, 77–88.

18 M. A. Ahmed, M. F. Abdel-Messih and E. H. Ismail, Facile synthesis of novel microporous $CdSe/SiO_2$ nanocomposites selective for removal of methylene blue dye by tandem adsorption and photocatalytic process, *J. Mater. Sci.: Mater. Electron.*, 2019, **30**, 17527–17539.

19 R. Abdel-Aziz, M. A. Ahmed and M. F. Abdel-Messih, A novel UV and visible light driven photocatalyst $AgIO_4/ZnO$ nanoparticles with highly enhanced photocatalytic performance for removal of rhodamine B and indigo carmine dye, *J. Photochem. Photobiol., A*, 2020, **389**, 112245.

20 M. F. Abdel Messih, A. E. Shalan, M. F. Sanad and M. A. Ahmed, Facile approach to prepare $ZnO@SiO_2$ nanomaterials for photocatalytic degradation of some organic pollutant models, *J. Mater. Sci.: Mater. Electron.*, 2019, **30**, 1491–1499.

21 L. Chen, Q. Zhang, R. Huang, S. F. Yin, S. L. Luo and C. T. Au, Porous peanut-like Bi_2O_3–$BiVO_4$ composites with heterojunction: one-step synthesis and their photocatalytic properties, *Dalton Trans.*, 2012, **41**, 9513–9518.

22 H. Li, K. Yu, X. Lei, B. Guo, H. Fu and Z. Zhu, Hydrothermal synthesis of novel $MoS_2/BiVO_4$ hetero-nanoflowers with enhanced photocatalytic activity and a mechanism investigation, *J. Phys. Chem. C*, 2015, **119**, 22681–22689.

23 O. Yehezkeli, A. Harguindey, D. W. Domaille, L. He and J. N. Cha, Synthesis and phase transfer of well-defined $BiVO_4$ nanocrystals for photocatalytic water splitting, *RSC Adv.*, 2015, **5**, 58755–58759.

24 Z. Guo, P. Li, H. Che, G. Wang, C. Wu, X. Zhang and J. Mu, One-dimensional spindle-like $BiVO_4/TiO_2$ nanofibers heterojunction nanocomposites with enhanced visible light photocatalytic activity, *Ceram. Int.*, 2016, **42**, 4517–4525.

25 M. F. R. Samsudin, S. Sufian, R. Bashiri, N. M. Mohamed, L. T. Siang and R. M. Ramli, Optimization of photodegradation of methylene blue over modified TiO_2/$BiVO_4$ photocatalysts: effects of total TiO_2 loading and different type of co-catalyst, *Mater. Today: Proc.*, 2018, **5**, 21710–21717.

26 C. Ma and M. Wei, $BiVO_4$-nanorod-decorated rutile/anatase TiO_2 nanofibers with enhanced photoelectrochemical performance; Matters, *Lett*, 2020, **299**, 126849.

27 Y. R. Lv, C. J. Liu, R. K. He, X. Li and Y. H. Xu, $BiVO_4/TiO_2$ heterojunction with enhanced photocatalytic activities and photoelectochemistry performances under visible light illumination, *Mater. Res. Bull.*, 2019, **117**, 35–40.

28 Y. Hu, D. Li, Y. Zheng, W. Chen and G. Xiao, $BiVO_4/TiO_2$ nanocrystalline heterostructure: A wide spectrum responsive photocatalyst towards the highly efficient decomposition of gaseous benzene, *Appl. Catal., B*, 2011, **27**, 30–36.

29 Z. Guo, P. Li, H. Che, G. Wang and J. Mu, One-dimensional spindle-like $BiVO_4/TiO_2$ nanofibers heterojunction nanocomposites with enhanced visible light photocatalytic activity, *Ceram. Int.*, 2016, **42**, 4517–4525.

30 Z. K. Heiba, M. A. Ahmed and S. I. Ahmed, Structural investigations of nano mixed oxides SnO_2–xAl_2O_3 prepared by sol–gel technique, *J. Alloys Compd.*, 2010, **507**, 253–256.

31 M. A. Ahmed, E. S. Yousef and M. F. Abdel-Messih, Preparation and characterization of nanocomposites prepared in system as SnO_2-x TiO_2 (X=25, 50 and 75 mol%), *J. Sol-Gel Sci. Technol.*, 2011, **60**, 58–65.

32 A. H. Galal, M. G. El-mahgary and M. A. Ahmed, Construction of novel $AgIO_4/ZnO$/graphene direct Z-scheme heterojunctions for exceptional photocatalytic hydrogen gas production, *Nanotechnol. Environ. Eng.*, 2020, **6**, 5.

33 N. Al-Zaqri, A. Alsalme, M. A. Ahmed and A. H. Galal, Construction of novel direct Z-scheme $AgIO_4$-g-C_3N_4 heterojunction for photocatalytic hydrogen production and photodegradation of fluorescein dye, *Diam. Relat. Mater.*, 2020, **109**, 108071.

34 M. A. Ahmed, N. Al-Zaqri, A. Ali, A. H. Glal and E. Mahmood, Rapid photocatalytic degradation of RhB dye and photocatalytic hydrogen production on novel curcumin/SnO_2 nanocomposites through direct Z-scheme mechanism, *J. Mater. Sci.: Mater. Electron.*, 2020, **31**(21), 19188–19203.

35 H. Ma, W. Ma, J. F. Chen, X.-Y. Liu, Y.-Y. Peng, Z.-Y. Yang, H. Tian and Y.-T. Long, Quantifying Visible-Light-Induced Electron Transfer Properties of Single Dye-Sensitized ZnO Entity for Water Splitting, *J. Am. Chem. Soc.*, 2018, **140**, 5272.

36 J. Chen, S. Huang, Y. Long, J. Wu, H. Li, Z. Li, Y.-J. Zeng and S. Ruan, Fabrication of ZnO/Red Phosphorus Heterostructure for Effective Photocatalytic H_2 Evolution from Water Splitting, *Nanomaterials*, 2018, **8**, 835.

37 S. W. B. Zhu, M. Liu, L. Zhang, J. Yu and M. Zhou, Direct Z-scheme ZnO/CdS hierarchical photocatalyst for enhanced photocatalytic H2-production activity, *Appl. Catal., B*, 2019, **243**, 19.

38 S. Wageh, A. A. Al-Ghamdi, R. J. X. Li and P. Zhang, A new heterojunction in photocatalysis: S-scheme heterojunction, *Chin. J. Catal.*, 2021, **42**, 667–669.

39 Q. Xu, L. Zhang, B. Cheng, J. Fan and J. Yu, S-Scheme Heterojunction Photocatalyst, *Chem*, 2020, **6**, 1543–1559.

40 A. Meng, B. Cheng, H. Tan, J. Fan, C. Su and J. Yu, TiO_2/polydopamine S-scheme heterojunction photocatalyst with enhanced CO_2-reduction selectivity, *Appl. Catal., B*, 2021, **289**, 120039.

41 Y. Xiao, Z. Ji, C. Zou, Yi. Xu, R. Wang, J. Wu, G. Liu, P. He, Q. Wang and T. Jia, Construction of CeO_2/BiOI S-scheme heterojunction for photocatalytic removal of elemental mercury, *Appl. Surf. Sci.*, 2021, **556**, 149767.

42 Q. Li, W. Zhao, Z. Zhai, K. Ren, T. Wang, H. Guan and H. Shi, 2D/2D Bi_2MoO_6/g-C_3N_4 S-scheme heterojunction photocatalyst with enhanced visible-light activity by Au loading, *J. Mater. Sci. Technol.*, 2020, **56**, 216–226.

43 A. R. M. Shaheer, V. Vinesh, S. K. Lakhera and B. Neppolian, Reduced graphene oxide as a solid-state mediator in TiO_2/$In_{0.5}WO_3$ S-scheme photocatalyst for hydrogen production, *Sol. Energy*, 2021, **13**, 260–270.

44 S. Wu, X. Yu, J. Zhang, Y. Zhang, Y. Zhu and M. Zhu, Construction of BiOCl/$CuBi_2O_4$ S-scheme heterojunction with oxygen vacancy for enhanced photocatalytic diclofenac degradation and nitric oxide removal, *Chem. Eng. J.*, 2021, **411**, 128555.

45 S. Jiang, J. Cao, M. Guo, D. Cao, X. Jia, H. Lin and S. Chen, Novel S-scheme WO_3/RP composite with outstanding overall water splitting activity for H_2 and O_2 evolution under visible light, *Appl. Surf. Sci.*, 2021, **558**, 149882.

46 X. Zhang, Y. Zhang, X. Jia, N. Zhang, R. Xia, X. Zhang, Z. Wang and M. Yu, In situ fabrication of a novel S-scheme heterojunction photocatalyts Bi_2O_3/P-C_3N_4 to enhance levofloxacin removal from water, *Sep. Purif. Technol.*, 2021, **268**, 118691.

47 Q. Liu, X. He, J. Peng, X. Yu, H. Tang and J. Zhang, Hot-electron-assisted S-scheme heterojunction of tungsten oxide/graphitic carbon nitride for broad-spectrum photocatalytic H_2 generation, *Chin. J. Catal.*, 2021, **42**, 1478–1487.

48 K. Z. D. Li, Q. Tian, H. Cao, F. Orudzhev, I. A. Zvereva, J. Xu and C. Wang, Recyclable 0D/2D $ZnFe_2O_4$/$Bi_5FeTi_3O_{15}$ S-scheme heterojunction with bismuth decoration for enhanced visible-light-driven tetracycline photodegradation, *Ceram. Int.*, 2021, **47**, 17109–17119.

49 Y. Zhao, Y. Guo, J. Li and P. Li, Efficient hydrogen evolution with ZnO/$SrTiO_3$ S-scheme heterojunction photocatalyst sensitized by Eosin Y, *Int. J. Hydrogen Energy*, 2021, **46**, 18922–18935.